Electronic Supplementary Material (ESI) for Analyst.

Supplementary Information

Water Monitoring with an Automated Smart Sensor supported with Solar Power for Real-time and Long Range Detection of Ferrous Iron

Tugba Ozer [a,b,c,d*], Ismail Agir [e], Thomas Borch[b,c*]

[a] Department of Bioengineering, Faculty of Chemical and Metallurgical Engineering, Yildiz Technical University, 34220 Istanbul, Türkiye

[b] Department of Chemistry, Colorado State University, 1170 Campus Delivery, Fort Collins, CO 80523, United States

[c] Department of Soil and Crop Sciences, 1170 Campus Delivery, Fort Collins, CO 80523, United States

[d] Health Biotechnology Joint Research and Application Center of Excellence, 34220 Esenler, Istanbul, Türkiye

[e] Department of Bioengineering, Istanbul Medeniyet University, Faculty of Engineering and Natural Sciences, 34700 Istanbul, Türkiye

[*]Co-Corresponding authors:

Thomas Borch: Thomas.Borch@ColoState.edu

Tugba Ozer: tozer@yildiz.edu.tr

Experimental

Materials

High molecular weight poly(vinyl) chloride (HMW-PVC), carboxylated PVC (CPVC), dibutyl phthalate (DBP), dioctyl Phthalate (DOP), 2-nitrophenyl octyl ether (o-NPOE), bis(2-ethylhexyl) sebacate (DOS), sodium tetrakis-[3,5-bis(trifluoromethyl)phenyl]borate (NaTFPB), poly(butyl methacrylate-co-methyl methacrylate), tetra-dodecylammonium tetrakis(4-chlorophenyl)borate cyanomethyl N-methyl-N-phenyl dithiocarbamate were purchased from Fluka (USA). Vulcan XCMAX22 Carbon Black was purchased from Cabot Corporation (Boston, USA). Anhydrous and inhibitor free tetrahydrofuran (THF) at %99.9 (w/w) purity was purchased from Sigma-Aldrich (USA). Ultrapure deionized water (Milli-Q, 18 MΩ cm) was used throughout the experiments. During the preparation of anoxic solutions, water was purged with oxygen-free nitrogen gas for 1 h while boiling and stirring. All standard solutions were prepared from commercial analytical grade nitrate or chloride salts (Fisher Chemical, USA) of the related cations. The diluted solutions of metal salts were prepared from their stock solution of 0.1 M with adequate amount of ultrapure deionized water. 1,4-Piperazinediethanesulfonic acid (PIPES) (Acros Organics, USA) and HNO_3 (Fisher Chemical, USA) were used for adjusting the pH of the solutions.

Apparatus

A smartphone assisted lab-made potentiometer with its customized application was used to carry out the potentiometric measurements. HI9126 (Hanna Instruments) waterproof portable pH/mV meter including the HI1230B double junction pH electrode was used to monitor the pH and redox potential of the solutions. Branson ultrasonic bath (USA) was used to homogenize solutions. Inductively coupled plasma optical emission spectrometry (ICP-OES) (Hitachi, MA, USA) was used for analysis of Fe in samples.

Surface characterization of Fe^{2+}-selective electrode

The surface morphology of Fe^{2+}-selective electrodes was obtained using scanning electron microscopy (SEM) on a JEOL JSM-6500F field emission electron microscope at an accelerating voltage of 5.0 kV for imaging and either 10.0 or 15.0 kV for SEM EDS using an Oxford X-Max 80 mm2 EDS detector. X-ray photoelectron spectroscopy (XPS) was used to characterize the ISM modified on the SPCE before and after conditioning process. The XPS is a Physical Electronics (PHI) 5800 series Multi-Technique ESCA system with a monochromatic Al Kα ($h\nu$ = 1486.6 eV) source and is operated at 350.0 W. An electron flood gun was used for charge neutralization. High resolution scans were collected with a pass energy of 23.5 eV and an interval of 0.1 eV/step.

Microfluidic chamber design

Using Autodesk Inventor 2023 software, we fabricated a microfluidic chamber to integrate with the developed sensor while adjusting the pH of the sample with a buffer solution. The pressure of the pumps as the driving force was used to effectively mix water sample with the pH buffer in the mixing chamber. A micromixer geometry with a high mixing performance (mixing index) was used to design the mixing chamber and resemble a sinusoid signal in a multi-wave topology (Chen et al. 2017). The inlet and outlet ports include 3 mm of inner diameter tubing. As shown in Figure S1, a transparent PETG filament (Microzey, Turkey) was used to fabricate the device using a 3D printer at a nozzle temperature of 235 °C in two parts (top and bottom) with a layer height of 0.1 mm. To improve the transparency of the final product, the default print speed and the extrusion multiplier were set to 15 mm/s (1/4 of the standard speed) and 1.05 mm/s, respectively, while the default infill print angle offsets were set to zero to extrude all lines in parallel. To prevent any leakage when in contact with a liquid sample, clear double-sided tape was applied between the two parts and then tightened using bolt-nuts (Maharbiz et al. 2004). The solutions of Fe^{2+} with different concentrations in a range of 1×10^{-1}- 1×10^{-6} M were freshly prepared, and their pH values were adjusted with piperazine-N,N′-bis(2-ethanesulfonic acid) and HNO_3 solutions. The activity coefficients were calculated by converting concentration to activities according to the Debye–Huckel equation (Kontogeorgis et al. 2018).

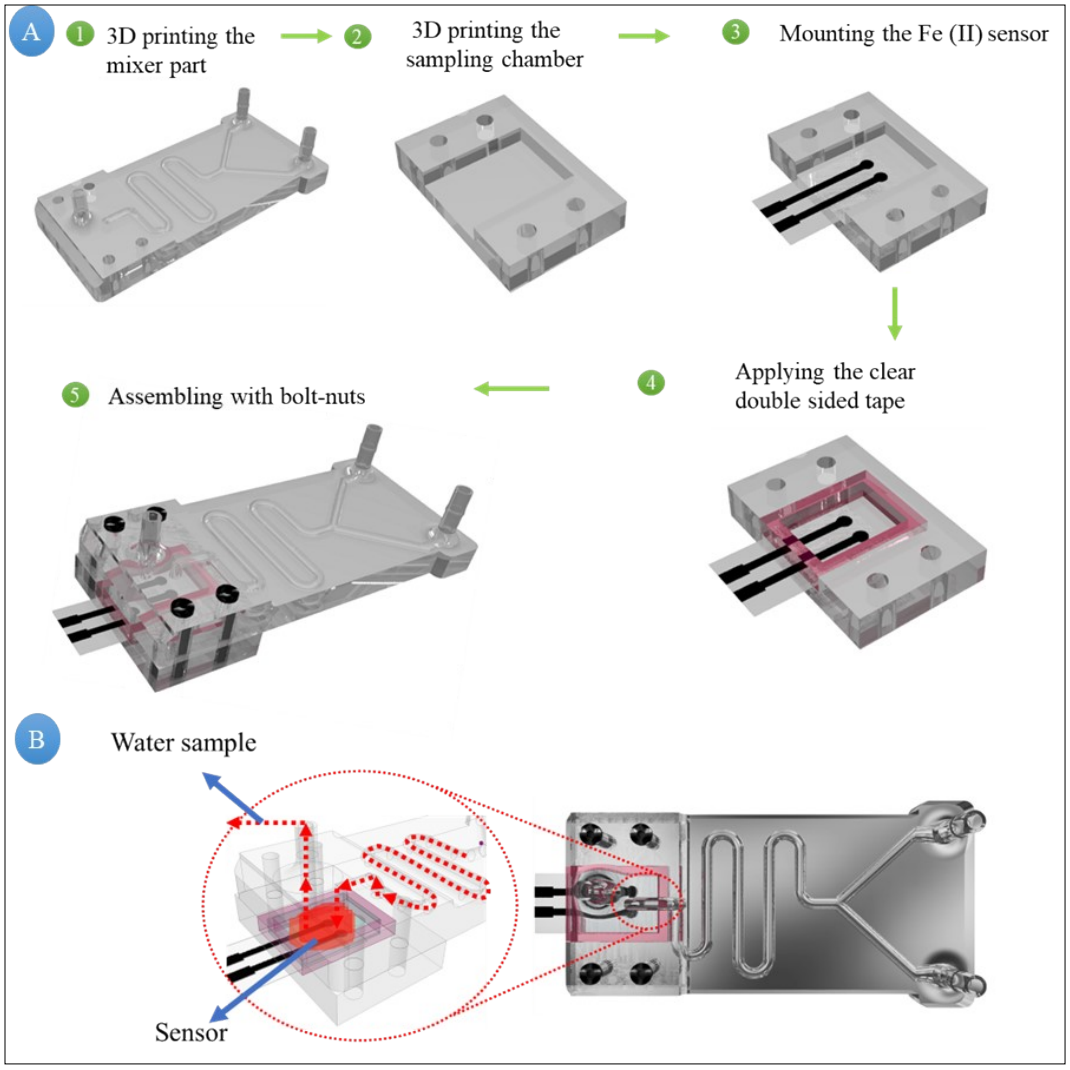

Figure S1. (A) Fabrication steps of the 3D-printed microfluidic chamber, (B) a close-up view of the sensor in contact with the water sample.

Components of the sensing platform

The fully custom-made floating platform consists of an energy supply and control unit, a microfluidic chamber including microfluidic mixing part, a pH buffer pump and container, DC and servo motors, an immersible pump, a propeller and flaps, a hose reel mechanism made with an empty (reusable) 3D filament spool, a reference image printed on paper that allows augmented reality contents to be anchored on it, an analog front-end circuit, a microcontroller and peripherals as communication module and motor driver. The highlighted features of the sensing platform are summarized in the Figure S2.

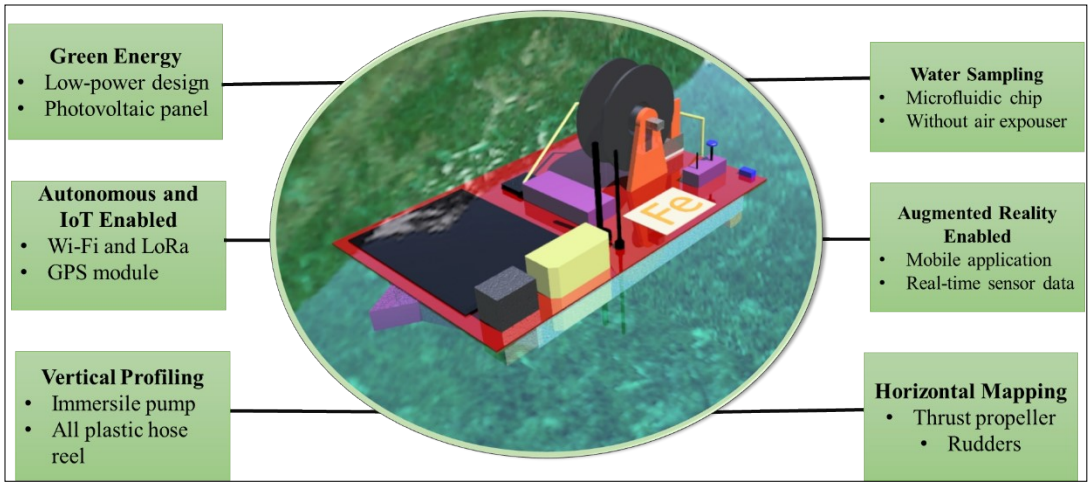

Figure S2. Features of the platform for detection of Fe^{2+} ion in water sources.

Hose reel and sampling mechanism

A winch-like hose reel system was installed on the platform to move the submersible pump into the water at adjustable depths. The parts of the assembled system are shown in Figure S3, we used 3D printer filament spool as the hose reel. A PVC pipe with 6 mm outer and 3 mm of inner diameter was used as the hose. The system design and assembly steps are given in Figure S4. Since the place where the hose on the rotable reel connects to the platform was fixed, the pipe was not able to twist incrementally with each turn. To tackle with this issue, rotary unions (or swivel joints) and a "slip ring" (2 pin) for the connection of the submersible motor cable were used in water transfer systems from a rotating point to a fixed location (Lakshminarayanan 2021). A rotary union was fabricated with a 3D FDM printer using PETG filament (Porima, Turkey) to prevent liquid contact with any metal in our system. A high torque DC motor controlled using a LN298N driver module (STMicroelectronics, Switzerland) was used to rotate the spool and determine the depth to be sampled. Two meters of hose and electrical cable were wound on the reel. The depth of the sampling unit was adjusted using a vertical profiling algorithm, taking into account the diameter of the rolled-up hose changing while the stepper motor rotates. A mini DC pump was operated with the LN298N (STMicroelectronics, Switzerland). The flow rate of the water sample was adjusted via PWM signal from the ESP32 microcontroller (Yin et al. 2016). At the water inlet of the submersible pump, the floating solids were fitted by adding a plastic sieve with 0.2 mm holes fabricated using the 3D- printer. The electronic circuit diagram of the water sampling system is given in Figure S5.

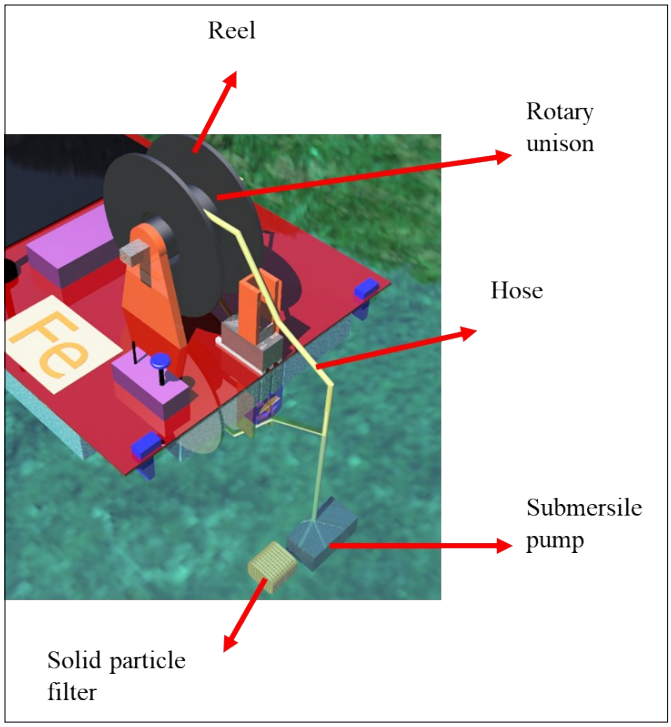

Figure S3. Components of the water sampling system.

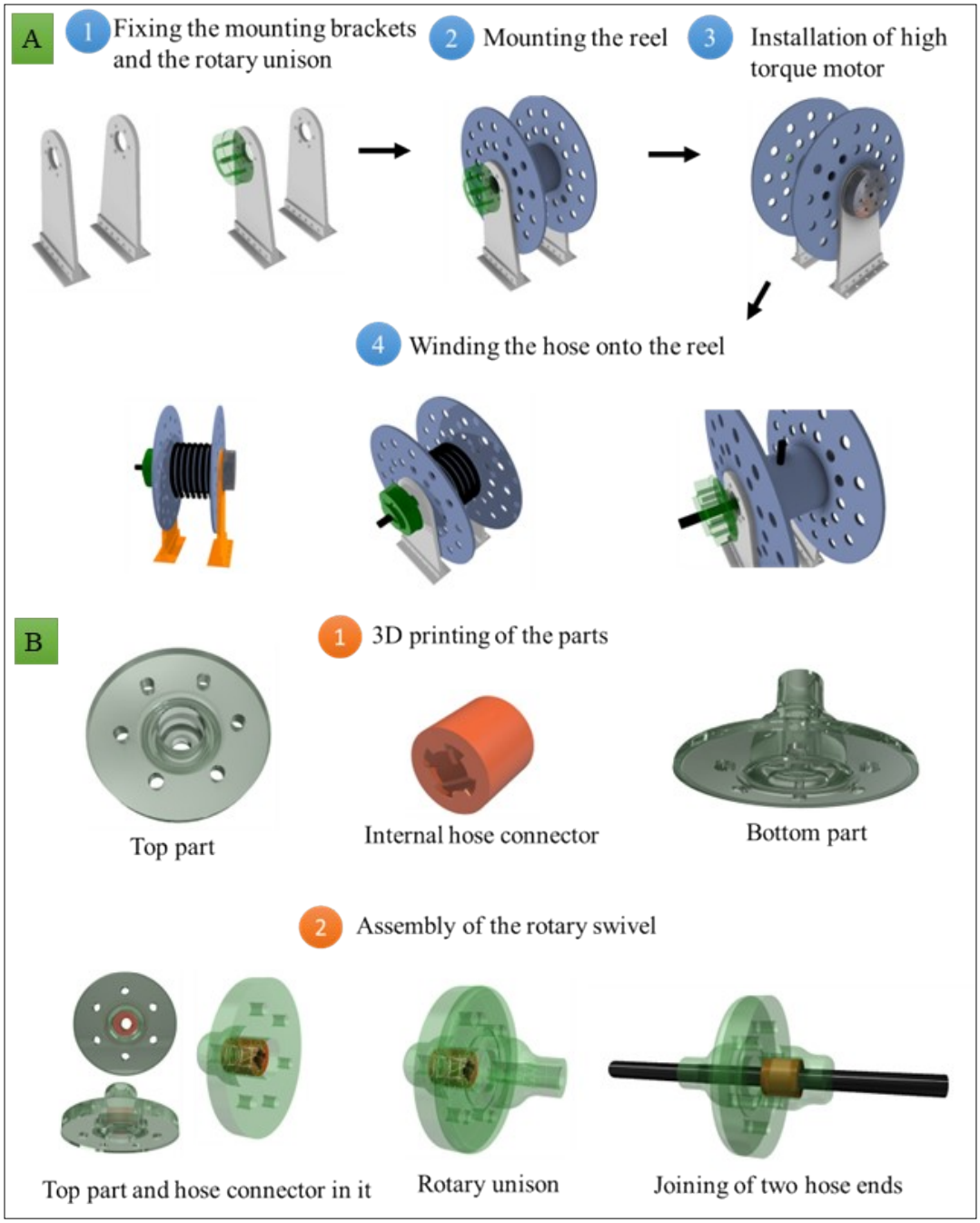

Figure S4. (A) Fabrication steps of hose reel system, (B) assembly of the 3D printed all plastic rotary unison.

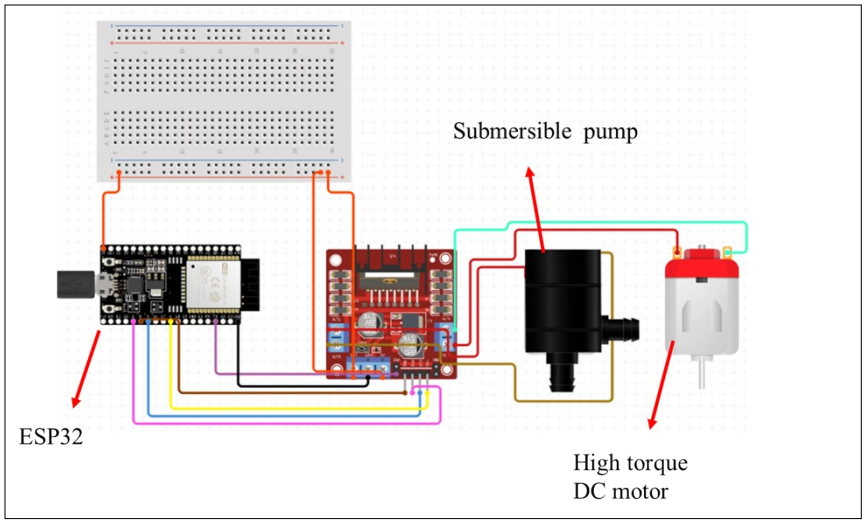

Figure S5. Electronics scheme of the water sampling system.

Implementing Long Range Wireless Communication and Internet of Things (IoT)

The LoRa connectivity is included in our proposed system so that iron levels can be remotely monitored, and the data can be transferred to ThingSpeak server which can be accessed from any location by experts. A hybrid wireless connectivity network for our floating platform by combining LoRa and Wi-Fi protocols is shown in Figure S6 (Ahsan et al. 2021). This hybrid network enables the communication with the platform up to 10 km in line of sight with a low-power consumption. The microcontroller was programmed to turn off the Wi-Fi radio and communicate with LoRa when the distance between the platform and the mobile phone is more than 30 m or by polling the RSSI value to ensure that it is not less than -90 dBm. In addition to the embedded Wi-Fi of the microcontroller (ESP32) to enable LoRa, a LoRa module based on the SX1278 (Semtech, USA) with a frequency band of 433 mHz and transmit power of 30dBm (1W) was connected to the UART port of the microcontroller (baud rate is 9600 bits/second). A hybrid Wi-Fi - LoRa intermediate station was developed to connect the smartphone to LoRa. The LoRa data transfer rate was set to 2.4 kbps and generated peer-to-peer communication using plain-text protocol. A UDP server was set up using a DatagramSocket class (Java) in the smartphone application algorithm. Communication was performed over the UDP port using the ESP32 Wi-Fi library in the embedded system. Address management capability was provided by setting up a handshake algorithm at both ends of the UDP listeners (Gu and Grossman 2007). Once the response of the embedded software received the first verification message, it was evaluated and verified by a smartphone. Then, this message was registered as a new sensor node with its IP address. Due to the generated command words, calibration process can be performed over the network. The application is able to convert mV values to the activities by using the Nernst equation using the Apache Commons Math library (Gordaliza et al. 2015). In addition, the application is able to keep the data in the phone memory and transmit to the cloud storage using HTTP GET (ThingSpeak.com) with GPS coordinates

and time information (datetime) (Pujara et al. 2020). ThingSpeak API parameters in embedded code are given in Figure S9.

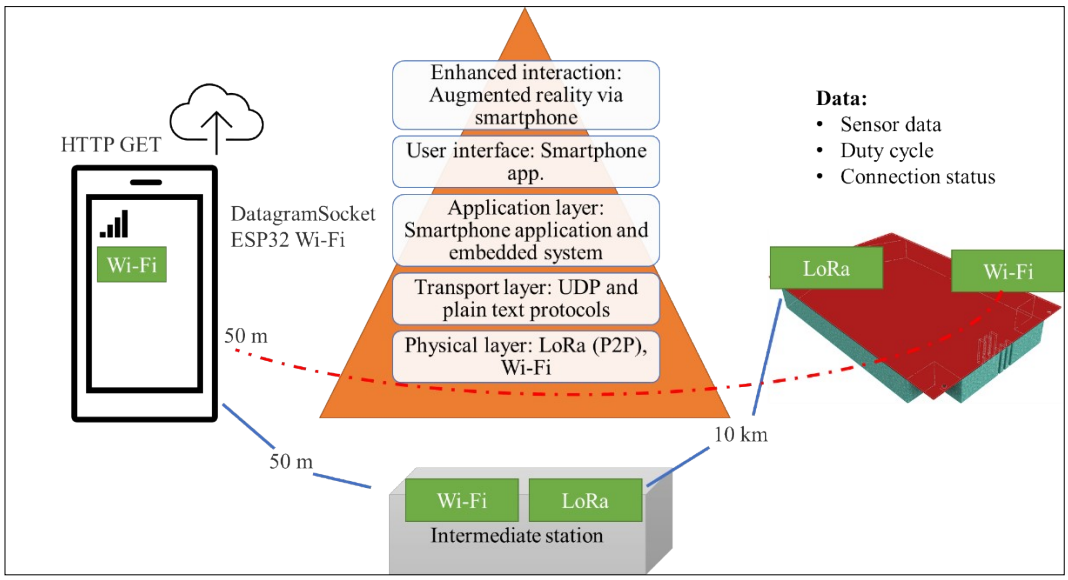

Figure S6. Block diagram of the hybrid network.

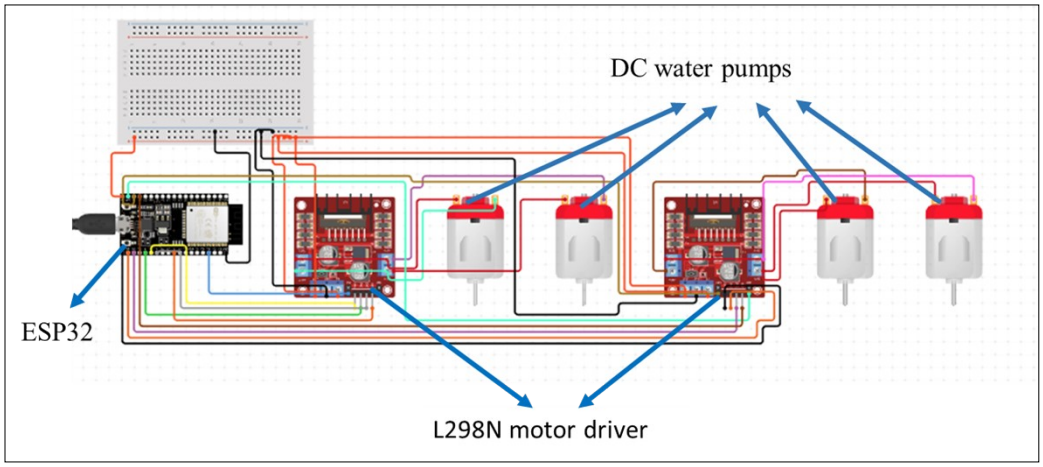

Figure S7. Circuit diagram of the automatic calibration system.

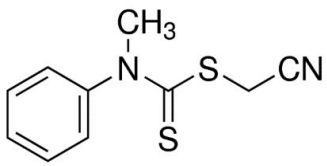

Figure S8. Structure of Cyanomethyl N-methyl-N-phenyl dithiocarbamate.

```
#include "ThingSpeak.h"
#include <WiFi.h>
...
unsigned long myChannelNumber = first_trial;
const char * myWriteAPIKey = "XXXXXXXXXXXXXXXX";
WiFiClient  client;
...
void setup() {
 ThingSpeak.begin(client);
}
...
void loop() {
...
ThingSpeak.writeField(myChannelNumber, 1, FE_ISE, myWriteAPIKey);
ThingSpeak.writeField(myChannelNumber, 2, timeStamp , myWriteAPIKey);
...
...
```

Figure S9. Firmware codes to run ADC and the schematic of the analog front-end circuit.

Analog front-end and measurement circuit of the portable potentiometer for EMF measurements

Ion selective electrodes generate EMF at high output impedance (>1 TOhM) and a typical analog-to-digital converter or a multimeter have considerably lower input impedance (<100 Kohm) (Hu et al. 2016). Therefore, there is a need to reduce the ISE output potential impedance without affecting the signal. The impedance conversion called as buffering is performed with electronic integrated circuits (IC) namely operational amplifiers (op-amp) (Madou and Morrison 2012). As shown in Figure S10, a potentiometer circuit (analog front-end) was designed to read the EMF signal of the sensor with a low noise op-amp, LMP7721 (TI, USA). Since an additional voltage gain is not required, the op-amp of the ISE in a unity gain (1:1) or voltage follower topology was configured (Mancini 2009a). The circuit was battery powered through a low-noise low drop-out voltage regulator (3V, TPS7A20, TI, USA). Due to the presence of a single battery, the op-amp is operated with a single-supply voltage (battery's ground to 3V) and EMF potentials generated by ISE below ground (0V) can not be measured unless there is a DC shifting or bias. A precision micro-power low-drop voltage reference IC (LM4140ACM-1.0/NOPB, TI, USA) to create a virtual ground at 1024 mV (Mancini 2009b) was used. This reference voltage was introduced to the system with another op-amp LMP7715 (TI, USA). Then, all the ICs on a breadboard using eight pin SOIC to DIP socket adapters was mounted. A 100 nF capacitor placed next to the supply pins to suppress possible noise in the power supply and deal with transients (Mitzner 2009) was added as well. An ADS1113 module (TI, USA) with 16-bit resolution as an analog-to-digital converter (ADC) with low current consumption (down to 150 µA) was used. The ADC operates within 0-4096 mV range, allowing the system measure in 0.0625 mV steps. The ADC was connected to the microcontroller via I^2C. The firmware codes of the ADC and the schematic of the analog front-end circuit are presented in Figure S11.

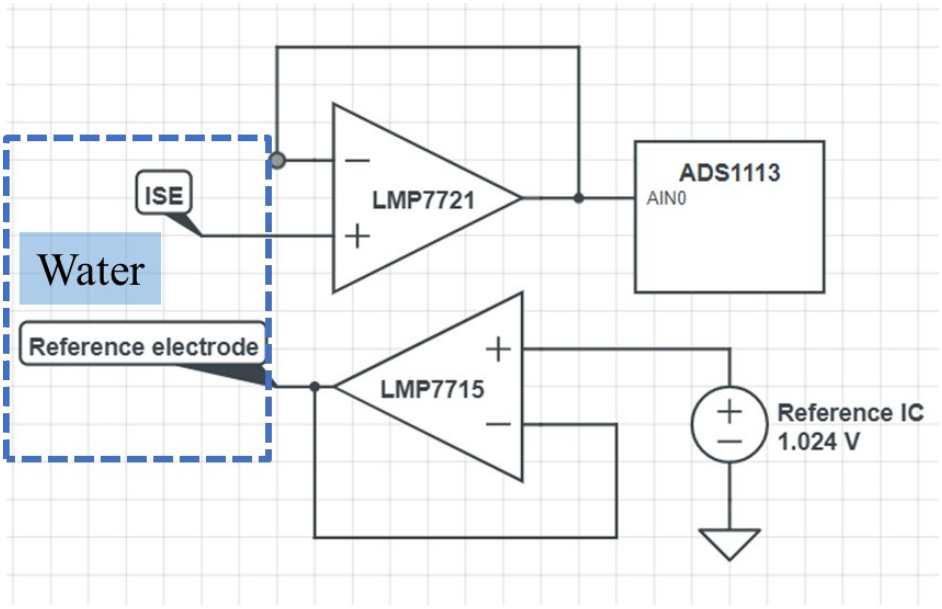

Figure S10. Block diagram of the portable EMF reader

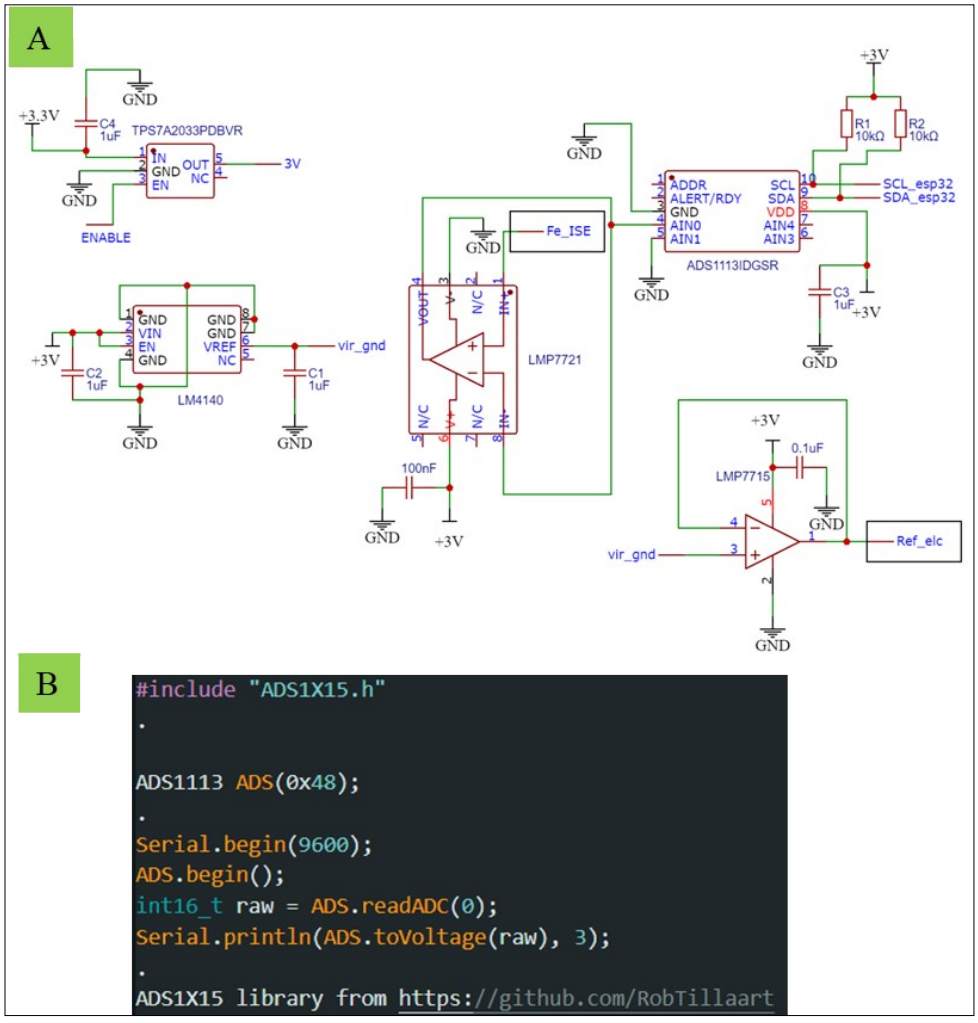

Figure S11. Circuit schematics of the analog front-end and example firmware codes of the ADC.

Floating boat body and GPS positioning

An autonomous moving floating platform was designed for in-situ sensor measurement using GPS and IoT. All electronic parts are lead-free (NOPB) and reusable due to the awareness of green environment. A 5 cm thick EPP (expanded polypropylene foam) (Labriola and Tagarielli 2007) sheet was selected due to its properties such as environmentally-friendly, sunlight resistive and mechanically strong. A 3 mm thick PMMA sheet was mounted on the top layer of the floating platform. In the location management of the platform, the Ardupilot kit and software "Mission Planner" as a ready-to-use open source development kit were used (Hassan et al. 2017). This kit was built-in GPS, telemetry and motor drivers, allowing automatic motion. To provide maneuverability to the platform, two flaps (or fins) were fabricated using a 3D-printer and corn syrup origin "Tough PLA" filament (Porima, Turkey), and connected to the servo motor (Tower Pro MG996R). A triangular shaped water splitting equipment was added to the front side of the platform to pave the way for its movement on water. Also, a propeller fabricated with a 3D printer motor was connected to the thruster. The block diagram containing all the parts of the system is given in Figure S12.

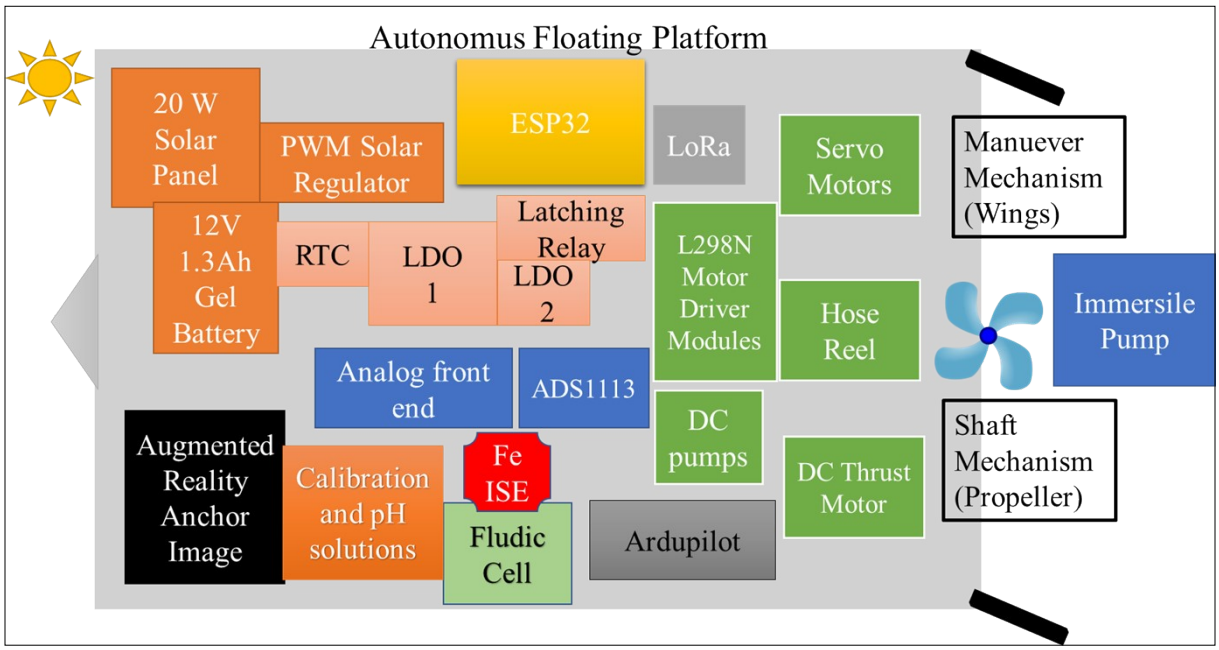

Figure S12. Functional diagram consisted of all the parts of the floating platform.

Embedded system

To manage the platform for data communication, power and network control; an ESP32 module (ESP32-S3-DevKitC-1-N8, Espressif Systems) was used as a microcontroller since it has low power consumption, sufficient number and variety of digital and analog input and output pins (GPIO), and built-in Wi-Fi. The embedded system diagram of the microcontroller is given in Figure S13. The module

in C++ with the Arduino IDE was programmed using ESP-IDF. With the embedded system software on ESP32, algorithms were generated for management of duty cycle, data acquisition, data communication, automatic calibration, and measurement of sensors with a microfluidic system.

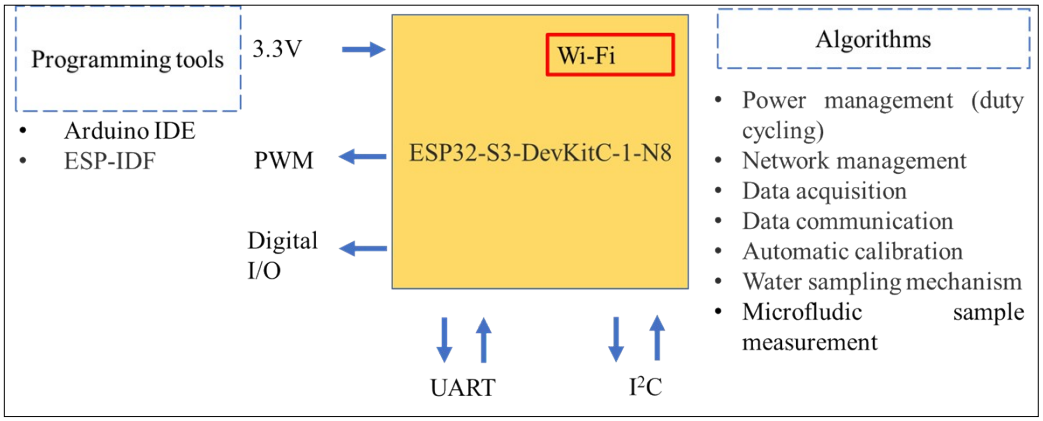

Figure S13. Functional diagram of the embedded system.

Green energy

The platform was designed to meet green energy and sustainability goals (Nižetić et al. 2020). As shown in Figure S14, solar energy as a power source was used by adding a photovoltaic energy harvesting panel (20 W) (Ghaib and Ben-Fares 2017, Mayer et al. 2020). A 12V 1.3 Ah lead-acid battery was connected to an OEM brand 20A PWM solar battery (charge) regulator and used as the energy storage. A I²C programmable, ultra-low-power (60 nA) real-time clock (RTC) module RV-3028-C7 (Micro Crystal AG, Switzerland) connected to a low noise low-dropout regulator (LT1963A, Analog Devices, USA) with a SHUTDOWN pin and a quiescent current consumption of 10 nA were added. The microcontroller was also added to the photovoltaic energy harvesting panel (20 W) by connecting the LT1963A's V_{out} to its V_{in} pin. The microcontroller was programmed to control a lead-acid battery-connected latching relay module (SRD-05VDC-SL-C, Ningbo Songle Relay, PRC) to power the motor drivers after boot. Latching relays do not need power to maintain their state after switching (Kang et al. 2011). A 10A fuse was connected to the battery output to prevent short circuit for safety measures. Finally, a precision low dropout voltage regulator (TPS7A20, Texas Instruments, USA) with 7 nA quiescent current was used to power the analog signal chain and its ENABLE pin was controlled by the microcontroller. With this configuration, the system consumes under 100 nA (at 3.3V) current in deep sleep (quiet state, when shut down).

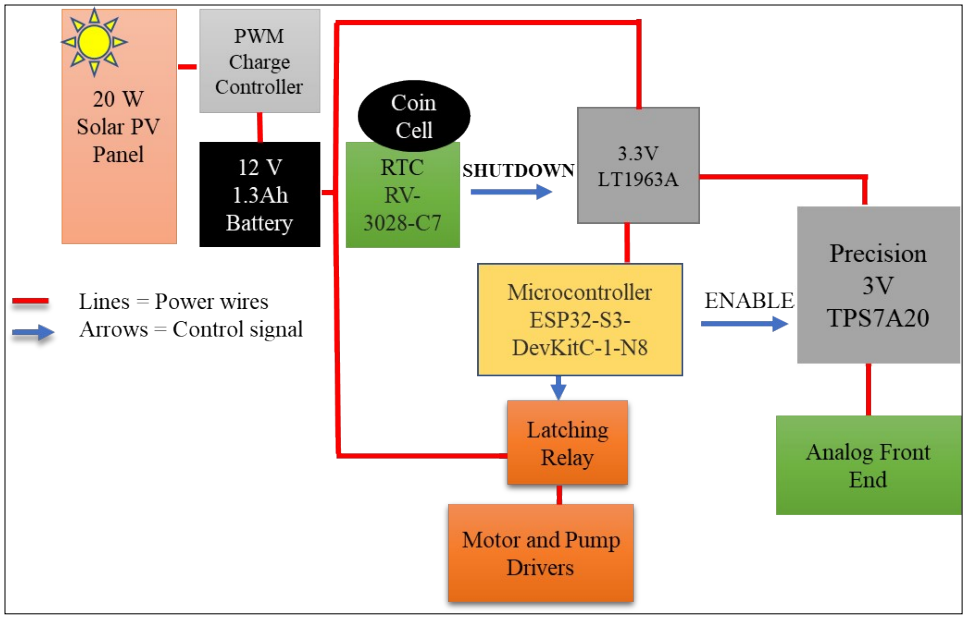

Figure S14. Functional diagram of the green energy power unit.

Augmented reality supported Android application

Here, IoT and augmented reality enabled smartphone application for Android devices were developed. Android Studio Chipmunk | 2021.2.1 and Java programming language were used. There are various types of augmented reality concepts (Berryman 2012). For example, superimposition-based augmented reality is able to add another image onto the image seen by the human eye (Bowskill and Downie 1995). Another common augmented reality application could place various digital information cards such as sensor data, in the form of 2D and 3D virtual images in real time, over the video taken from the camera with a smartphone or glasses (Carmigniani et al. 2011). To provide fundamental augmented reality experience, the ARcore platform supported by Android 7.0 and newer versions was used (Oufqir et al. 2020). The ARcore has the capability of the motion tracking and artificial intelligence (AI) based image recognition for placing both 2D and 3D objects on the layer of real world images in real-time. With the Augmented Images API in ARcore, the target (reference) image (anchor) placed on the platform was introduced by computer vision, and the location of the sensor data card was determined and tracked in real-time. The reference images were generated and converted to the image database files by the “arcoreimg” tool (.imgdb). The reference image on A4 size paper was designed and placed it on the platform as shown in Figure S15. In order to continuously display the sensor's data with augmented reality, there is a need to create real-time 2D images (cards). Therefore, we used Sceneform 1.15.0 framework and its “Renderable” class to render the sensor card. Receiving the real-time sensor data from the platform was over the UDP port as previously mentioned in the "Implementation of Long Range Wireless Communication and IoT" section. Also, we used Geospatial anchor references (included in the ARCore Geospatial API) to implement location-based augmented reality and rendered recorded data from the cloud (ThingSpeak) as a 2D sensor information card (image) on live camera video.

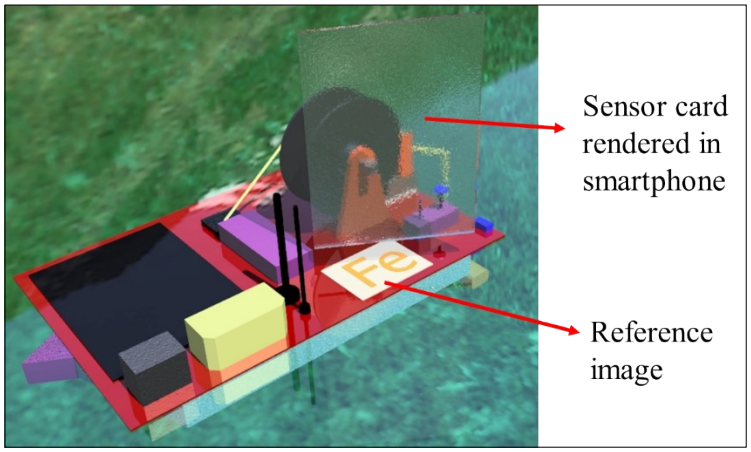

Figure S15. Floating platform with the printed reference image.

ARCore is simultaneously able to detect 20 reference images. Thus, it is possible to give unique identity (address) to different sensor nodes in an augmented reality environment. The designed reference images and their quality scores given by the arcoreimg tool are presented in Figure S16.

The augmented reality algorithm was created with the following steps:

1-ARcore is activated and camera usage permission is obtained.

2-UDP listener is initialized.

3-The target image of the computerized view is loaded and scanning/following is started, respectively. "Config.FocusMode" is set as "AUTO" to focus the camera optionally.

4-Once the picture is recognized, it is mapped to the identity of the data coming from UDP.

5-Incoming data is processed to create a layout (data card) using Sceneform.

6-The renderable object (data card) is real-time updated with the incoming data.

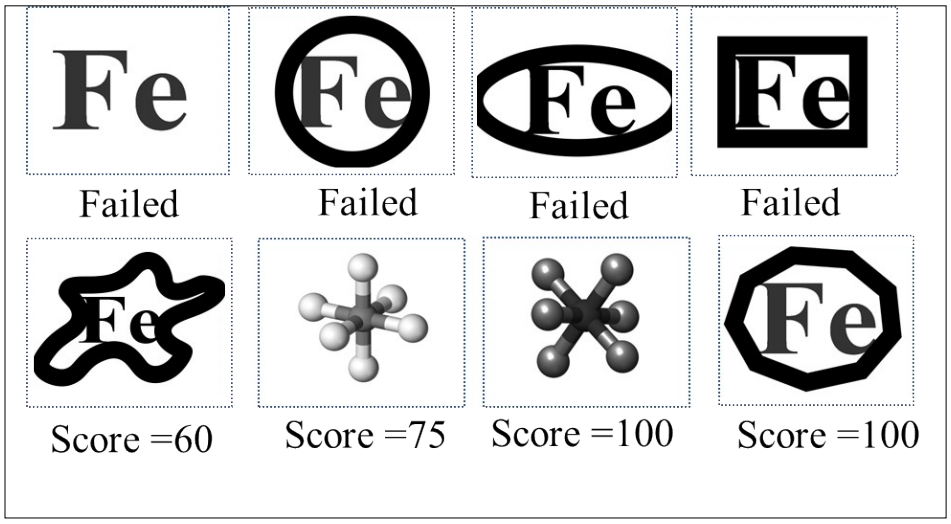

Figure S16. Various reference images and their quality scores.

Table S1. Compositions and response characteristics of the ISE including 4% (w/w) ionophore.

No	PVC (w/w %)	Plasticizer (w/w %)	Additive (w/w %)	Linear range (M)	Slope mV/decade
1	CPVC (30.0)	NPOE (65.0)	NaTPB (1.0)	1.0×10^{-1}-1.0×10^{-5}	29.76±0.60
2	HMW-PVC (30.0)	NPOE (65.0)	NaTPB (1.0)	1.0×10^{-1}-1.0×10^{-5}	22.3±0.3
3	CPVC (30.0)	DOS (65.0)	NaTPB (1.0)	1.0×10^{-2} to 1.0×10^{-5}	19.4±0.5
4	CPVC (30.0)	NPOE (66.0)	NaTPB (0)	1.0×10^{-2} to 1.0×10^{-5}	11.5±0.5
5	CPVC (30.0)	DOP (65.0)	NaTPB (1.0)	1.0×10^{-2} – 1.0×10^{-4}	32.3±0.2
6	CPVC (30.0)	DBP (65.0)	NaTPB (1.0)	1.0×10^{-3} – 1.0×10^{-5}	40.3±0.6

Table S2. All features of the platform.

Weight	3 kg.
Dimensions	60 x 100 x 6 cm body.
Specifications of the motors	Servo's (Tower Pro MG996R) stall torque: 9.4 kgf·cm. Thrust motor's (RS555) torque: 22.5 mN.m. Reel spinner motor's torque: 5 mN.m.
Battery capacity	1.3 Ah.
Power of the solar panel	20W/h.
Turning angle	30 °.
Diameter of the turning circle	6 meters.
Microfluidic system	Designed for mixing pH buffer solution with water samples and preparing them for measurement.
Duty cycle algorithm	Programmed for reducing overall energy consumption in the data acquisition system.
Standalone photovoltaic power supply	Harnesses solar energy to provide green electricity for the platform.
Augmented reality	Enabled real-time observation of sensor data using a smartphone camera and accessing readings from a database.
LoRa and Wi-Fi technology	Utilized for reliable wireless data transmission.

Assessment of Eco-scale

The floating measurement platform was designed with the goal of minimizing environmental impact and energy consumption while providing reliable in-situ measurements. To validate our approach towards environmental sustainability, we utilized an analytical calculation method known as the Eco-

Scale (Table S3). In the Eco-Scale method, penalty points were assigned to indicate potential environmental damage, which were then subtracted from 100 to determine the final score. By providing in-situ measurement with miniaturized sensor and microfluidic system, our approach eliminates the need for sample collection, preservation, transport, and storage. In this way, we conducted the preparation step prior to measurement within the microfluidic chip, thereby enabling direct analysis. Furthermore, the analytical calibration was performed without the need of any external intervention. Additionally, we aim to minimize energy consumption, with the use of the platform that require less than 0.1 kW per hour to perform at least 10 measurements at various locations. Our approach results in no gas emissions to the atmosphere, and the waste has no harm to the environment.

Table S3. Penalty point determination table according to the Eco-Scale metric.

Reagents	**Penalty point**
Hazard	
Tetrahydrofuran	6
High molecular weight poly(vinyl) chloride (HMW-PVC)	1
Carboxylated PVC (CPVC)	1
Dibutyl phthalate	4
2-nitrophenyl octyl ether (o-NPOE)	0
Bis(2-ethylhexyl) sebacate (DOS)	0
Sodium tetrakis-[3,5-bis(trifluoromethyl)phenyl]borate (NaTFPB)	0
Poly(butyl methacrylate-co-methyl methacrylate)	0
Tetra-dodecylammonium tetrakis(4-chlorophenyl)borate	1
cyanomethyl N-methyl-N-phenyl dithiocarbamate	0
Carbon black	0
1,4-Piperazinediethanesulfonic	0
Water	0
Instruments	

Energy	0
Occupational hazard	0
Waste	0
Total	13

References

Ahsan, M., Based, M.A., Haider, J. and Rodrigues, E.M. (2021) Smart monitoring and controlling of appliances using LoRa based IoT system. Designs 5(1), 17.

Berryman, D.R. (2012) Augmented reality: a review. Medical reference services quarterly 31(2), 212-218.

Bowskill, J. and Downie, J. (1995) Extending the capabilities of the human visual system: An introduction to enhanced reality. ACM SIGGRAPH Computer Graphics 29(2), 61-65.

Carmigniani, J., Furht, B., Anisetti, M., Ceravolo, P., Damiani, E. and Ivkovic, M. (2011) Augmented reality technologies, systems and applications. Multimedia tools and applications 51(1), 341-377.

Chen, X., Li, T. and Hu, Z. (2017) A novel research on serpentine microchannels of passive micromixers. Microsystem technologies 23(7), 2649-2656.

Ghaib, K. and Ben-Fares, F.-Z. (2017) A design methodology of stand-alone photovoltaic power systems for rural electrification. Energy Conversion and Management 148, 1127-1141.

Gordaliza, P., Mateos-Pérez, J.M., Montesinos, P., Guzmán-de-Villoria, J.A., Desco, M. and Vaquero, J.J. (2015) Development and validation of an open source quantification tool for DSC-MRI studies. Computers in Biology and Medicine 58, 56-62.

Gu, Y. and Grossman, R.L. (2007) UDT: UDP-based data transfer for high-speed wide area networks. Computer Networks 51(7), 1777-1799.

Hassan, S., Alam, M., Siddiqui, N.A., Siddiqui, A.A. and Qadri, M.T. (2017) Designing and control of autonomous Unmanned Ground Vehicle, pp. 1-5, IEEE.

Hu, J., Stein, A. and Bühlmann, P. (2016) Rational design of all-solid-state ion-selective electrodes and reference electrodes. TrAC Trends in Analytical Chemistry 76, 102-114.

Kang, S., Park, K., Shin, S., Chang, K. and Kim, H. (2011) Zero standby power remote control system using light power transmission. IEEE transactions on Consumer Electronics 57(4), 1622-1627.

Kontogeorgis, G.M., Maribo-Mogensen, B. and Thomsen, K. (2018) The Debye-Hückel theory and its importance in modeling electrolyte solutions. Fluid Phase Equilibria 462, 130-152.

Labriola, C. and Tagarielli, V. (2007) ARPRO®: A New Structural Core Material for the Yacht Industry, OnePetro.

Lakshminarayanan, S.P. (2021) Reliability analysis of rotary unions on balanced machines, pp. 1-5, IEEE.

Madou, M.J. and Morrison, S.R. (2012) Chemical sensing with solid state devices, Elsevier.

Maharbiz, M.M., Holtz, W.J., Howe, R.T. and Keasling, J.D. (2004) Microbioreactor arrays with parametric control for high-throughput experimentation. Biotechnology and bioengineering 85(4), 376-381.

Mancini, R. (2009a) Op Amps for Everyone, pp. 231-257, Elsevier.

Mancini, R. (2009b) Op Amps for Everyone, pp. 35-59, Elsevier.

Mayer, P., Magno, M. and Benini, L. (2020) Smart power unit—mW-to-nW power management and control for self-sustainable IoT devices. IEEE Transactions on Power Electronics 36(5), 5700-5710.

Mitzner, K. (2009) Complete PCB design using OrCAD Capture and PCB editor, Newnes.

Nižetić, S., Šolić, P., González-de, D.L.-d.-I. and Patrono, L. (2020) Internet of Things (IoT): Opportunities, issues and challenges towards a smart and sustainable future. Journal of Cleaner Production 274, 122877.

Oufqir, Z., El Abderrahmani, A. and Satori, K. (2020) ARKit and ARCore in serve to augmented reality, pp. 1-7, IEEE.

Pujara, D., Kukreja, P. and Gajjar, S. (2020) Design and Development of E-Sense: IoT based Environment Monitoring System, pp. 1-5, IEEE.
Yin, L., Wang, F., Han, S., Li, Y., Sun, H., Lu, Q., Yang, C. and Wang, Q. (2016) Application of drive circuit based on L298N in direct current motor speed control system, pp. 163-169, SPIE.